

Conformal Generative Modeling on Triangulated Surfaces

Victor Dorobantu¹ Charlotte Borchers¹ Yisong Yue¹

Abstract

We propose *conformal generative modeling*, a framework for generative modeling on 2D surfaces approximated by discrete triangle meshes. Our approach leverages advances in discrete conformal geometry to develop a map from a source triangle mesh to a target triangle mesh of a simple manifold such as a sphere. After accounting for errors due to the mesh discretization, we can use any generative modeling approach developed for simple manifolds as a plug-and-play subroutine. We demonstrate our framework on multiple complicated manifolds and multiple generative modeling subroutines, where we show that our approach can learn good estimates of distributions on meshes from samples, and can also learn simultaneously from multiple distinct meshes of the same underlying manifold.

1. Introduction

The study of learning expressive generative models has seen increasing interest in recent years, owing to the emergence of approaches such as continuous normalizing flows (Rezende & Mohamed, 2015; Dinh et al., 2016; Papamakarios et al., 2021) and diffusion models (Sohl-Dickstein et al., 2015; Song et al., 2020). Such models have the ability to both efficiently draw samples from the learned distribution, as well as compute exact probabilities on the input space, making them useful for many applications in science and engineering from experiment design (Song et al., 2022) to inverse problems (Gao et al., 2021; Song et al., 2021).

A key challenge in many domains is that the distribution to be estimated lies on a complicated manifold, rather than in Euclidean space. Examples include modeling molecular activity (Chen et al., 2012; Shapovalov & Dunbrack Jr, 2011), robotic motion (Feiten et al., 2013), high energy physics (Brehmer & Cranmer, 2020), and brain activity

(Gerber et al., 2010). Moreover, many domains use discrete approximations of the true manifold (e.g., triangle meshes).

Our goal is to develop generative modeling approaches for complicated 2D surfaces in the case where the training data is represented using discrete mesh approximations. Existing work on Riemannian generative modeling typically operate on canonical manifolds such as spheres, tori, hyperbolic spaces, and matrix Lie groups (De Bortoli et al., 2022; Mathieu & Nickel, 2020; Lou et al., 2020; Katsman et al., 2021) or else require uncontrolled approximations via learned implicit surface representations (Rozen et al., 2021). The challenge of learning generative models directly on complicated meshes remains open.

Our contributions. We propose *conformal generative modeling*, a framework for generative modeling on Riemannian manifolds approximated by discrete triangle meshes. Our approach is based on establishing a conformal transformation between the source mesh and a target mesh that approximates a simple manifold such as a sphere (Springborn et al., 2008). Such a transformation amounts to a diffeomorphism between the two manifolds, subject to accounting for approximation error from the mesh discretization. Afterwards, one can use any generative model for simple manifolds as a plug-and-play subroutine, which we demonstrate empirically on eight complicated manifolds (which is significantly more than has been demonstrated by other Riemannian generative modeling approaches). Our implementation is available at github.com/vdorbs/spherical-generative-modeling.git.

A further benefit of conformal generative modeling is that it can learn simultaneously using data from multiple distinct meshes of the same underlying manifold. This benefit comes from the ability to establish alignments between the conformal transformations of the meshes on the unit sphere (e.g., Baden et al. (2018); Wang et al. (2006)), as shown in Figure 1. We demonstrate this ability empirically, using data from multiple distinct meshes to train a single generative model capable of generating data on unseen meshes.

2. Preliminaries & Problem Statement

Our approach uses topological equivalences to simple manifolds (e.g., closed 2D Riemannian manifolds with no “holes” are topological spheres). We first describe notation to de-

¹Department of Computing and Mathematical Sciences, California Institute of Technology, Pasadena, CA, USA. Correspondence to: Victor Dorobantu <vdoroban@caltech.edu>.

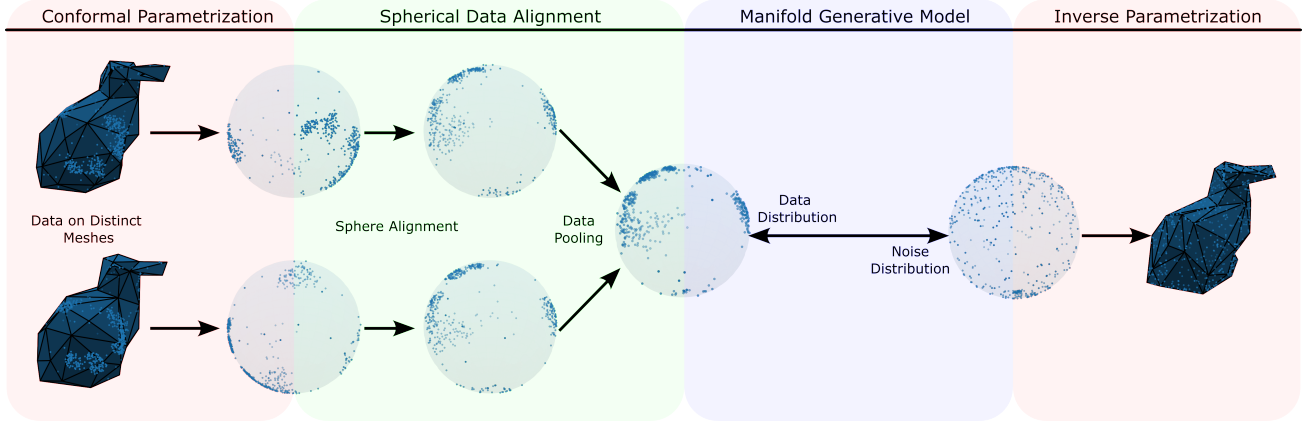


Figure 1. Overview of our approach. From left to right, original data samples are gathered from multiple meshes and mapped to unit sphere via discrete conformal transformations (red). The spheres are aligned with a reference mesh using rotations maximizing the correlation between log conformal factors, geometric signatures of the original meshes. Data is then aggregated on one sphere (green). A generative model transforms the data distribution on the sphere to a noise distribution on the sphere in the forward direction (blue). The resulting noise distribution is mapped to the reference mesh, again via a discrete conformal transformation. Here, the noise distribution on the reference mesh is uniform. Meshes are decimated to more clearly distinguish distinct meshes; for full meshes see Figure 5.

scribe such concepts and then the problem statement.

2.1. Notation, Definitions, and Conventions

Basics. We denote the unit two-sphere by S^2 . For manifold \mathcal{M} , we denote its tangent space at any $p \in \mathcal{M}$ by $T_p\mathcal{M}$. For manifolds \mathcal{M} and \mathcal{N} and a smooth map $f : \mathcal{M} \rightarrow \mathcal{N}$, we denote the differential of f at $p \in \mathcal{M}$ by $df_p : T_p\mathcal{M} \rightarrow T_{f(p)}\mathcal{N}$; this is a linear map between tangent spaces.

Triangle Meshes & Vertex Embeddings. A (Euclidean) triangle mesh is described by a triple $T = (V, E, F)$ and a vertex embedding $f : V \rightarrow \mathbb{R}^d$, where V is the set of vertices, E is a set of ordered vertex pairs comprising edges, F is a set of ordered vertex triples comprising faces, and $f_i \in \mathbb{R}^d$ denotes the position in space of vertex $i \in V$. As a simplicial complex, for each face in F , each pair of vertices must belong to the edge set E , potentially with the vertex order reversed. In this paper, we will exclusively consider *manifold* triangle meshes; in this case, each edge belongs to exactly two faces, with the exception of boundary edges (if they exist), which each belong to exactly one face. Such a triangle mesh is equipped with a *discrete metric* (the discrete analogue of a Riemannian metric) $\ell : E \rightarrow \mathbb{R}_{++}$:

$$\ell_{ij} = \|f_i - f_j\|_2. \quad (1)$$

This discrete metric must satisfy triangle inequality:

$$\ell_{ij} + \ell_{jk} \leq \ell_{ki}, \quad \ell_{jk} + \ell_{ki} \leq \ell_{ij}, \quad \ell_{ki} + \ell_{ij} \leq \ell_{jk}, \quad (2)$$

for each face $(i, j, k) \in F$.

Piecewise Linear Surfaces. Often we will need to consider the piecewise linear surface generated from a vertex embedding by placing triangle vertices at the vertex positions of

each face. We will typically denote such a surface as M ; we will assume available training data belongs to such surfaces.

Topological Equivalences. The mesh T is a topological sphere if it has no boundary and has an Euler characteristic $|F| - |E| + |V| = 2$ (i.e. has no “holes”). This implies only that T has the connectivity of a sphere (topological information), though not necessarily the geometry of one. If T is a topological sphere and $f_i \in S^2$ for each vertex $i \in V$, we will also consider *spherical* triangle meshes, which partition the sphere into spherical triangles.

A Riemannian manifold is a topological sphere if it is homeomorphic to a sphere; that is, if it admits a continuous bijection to the sphere with a continuous inverse.

2.2. Problem Statement

Consider a 2D Riemannian manifold \mathcal{M} that is a topological sphere. Our goal is to estimate a probability density function $\rho : \mathcal{M} \rightarrow \mathbb{R}_+$ using training samples generated i.i.d. from some underlying distribution on \mathcal{M} . We are generally interested in complicated manifolds (see Figures 1 and 4 for examples). Moreover, we assume that the training samples are represented on triangulated mesh approximations of \mathcal{M} .

Concretely, suppose we have access to n triangle meshes $T^{(1)}, \dots, T^{(n)}$ that approximate \mathcal{M} , with respective vertex embeddings $f^{(1)}, \dots, f^{(n)}$ and piecewise linear surfaces $M^{(1)}, \dots, M^{(n)}$. We assume the vertex embeddings place the vertices on \mathcal{M} . We also have access to n datasets, $\mathcal{D}^{(1)} \subset M^{(1)}, \dots, \mathcal{D}^{(n)} \subset M^{(n)}$, with each $\mathcal{D}^{(n)}$ comprising samples drawn i.i.d. from the underlying distribution on \mathcal{M} but represented spatially on $M^{(1)}, \dots, M^{(n)}$. Figure 1 (Left/Red) gives a depiction of the training data collected

on two distinct meshes of the Stanford Bunny surface.

3. Conformal Generative Modeling

Our *conformal generative modeling* framework is predicated on the idea of identifying an invertible transformation from each source mesh to the unit sphere.¹ Given such a transformation, training samples from each mesh are effectively transformed to form a single pooled set of (weighted) training samples on the unit sphere. Afterwards, one can use any existing Riemannian generative modeling approach estimate a probability density function on the sphere (Lou et al., 2020; Mathieu & Nickel, 2020; Rozen et al., 2021; De Bortoli et al., 2022). One can then invert the transformation to produce outputs on any of the meshes. Figure 1 presents a high-level depiction of our framework.

We first summarize the key steps, and then develop the necessary technical tools on conformal geometry, spherical parameterizations, and Möbius registration (Sections 3.1 & 3.2) to describe the full technical details of the approach (Section 3.3 and Algorithm 1).

Conformal Transformations & Conformal Factors. The specific type of transformations we will use are *discrete conformal transformations* (Springborn et al., 2008). Informally, conformal transformations are maximally angle-preserving² maps between two meshes (e.g., the source manifold and the sphere). In other words, for any two edges that share a vertex in common, the angle between those two edges are preserved as much as possible. A direct consequence is that the shape of each face on the mesh is also approximately preserved in the transformation. Importantly, however, conformal transformations may distort differential area. In doing so, a conformal transformation rescales edge lengths via a *conformal factor* at each vertex.

Aligning Multiple Meshes. In order to pool training data from multiple meshes, it is necessary to align their transformed meshes on the sphere, which amounts to finding a rotation of each mesh (Section 3.1.3). This step is skipped in the special case where we learn with only one mesh.

Creating Training Samples on the Sphere. In order to generate proper training examples on the sphere, two additional steps are needed. First, the conformal transformation has stretched or shrunk various parts of the source mesh, and so one must re-weight training samples in order to transport the original measure to the sphere. Intuitively, data points in

¹One could in principle compute transformations to other simple manifolds with higher Euler numbers, such as tori. However, certain algorithmic steps in the framework become more challenging, such as aligning the different meshes.

²Complete angle preservation overly restricts the class of admissible transformations, yielding only rigid isometries. See Crane (2020) for further discussion.

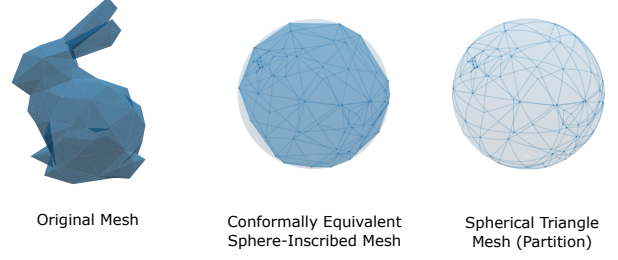


Figure 2. Correspondence between piecewise linear surfaces and unit sphere, with the original mesh on the left, the mesh after spherical parametrization in the center (shown inscribed within the unit sphere), and the associated partition of the sphere into spherical triangles on the right.

Algorithm 1 Conformal Generative Modeling

- input** Triangle meshes $T^{(1)}, \dots, T^{(n)}$ and corresponding piecewise linear surfaces $M^{(1)}, \dots, M^{(n)}$
- input** Training sets $\mathcal{D}^{(1)} \subset M^{(1)}, \dots, \mathcal{D}^{(n)} \subset M^{(n)}$
- 1: Compute conformal transformation from each mesh to the unit sphere (Section 3.1.2), obtaining $M_{\text{inscr}}^{(1)}, \dots, M_{\text{inscr}}^{(n)}$
 - 2: Align $M_{\text{inscr}}^{(2)}, \dots, M_{\text{inscr}}^{(n)}$ to $M_{\text{inscr}}^{(1)}$ with maximum correlation rotations (Equation (5))
 - 3: Map data to aligned spheres, obtaining $\tilde{\mathcal{D}}^{(1)}, \dots, \tilde{\mathcal{D}}^{(n)}$
 - 4: Compute log changes of area from projection (Equation (11)) and triangle area ratios for each data point in each of $\tilde{\mathcal{D}}^{(1)}, \dots, \tilde{\mathcal{D}}^{(n)}$
 - 5: Train likelihood-based generative model on sphere, subtracting log change of area from log probability densities in loss function (Equation (17))
 - 6: Return sphere generative model and inverse conformal transformations mapping to each of $M^{(1)}, \dots, M^{(n)}$
-

stretched portions should receive higher weight, and those in shrunk portions should receive lower weight.

The second step is to transform the linear triangle surfaces into spherical triangle surfaces. Figure 2 depicts this step, where the middle is a piecewise linear mesh that is circumscribed by the unit sphere (all the edges lie inside the sphere), and the right is a conversion of each triangle surface to a spherical one. It is straightforward to compose this transformation with the conformal transformation. In Section 3.1.2, we describe spherical parameterization, and in Section 3.2 we derive the additional differentiable change in area to compute an additional weighting factor for the training samples when transforming to a spherical mesh.

3.1. Background on Conformal Geometry

3.1.1. CONFORMAL EQUIVALENCE

Conformal maps locally preserve angles and orientations. Let \mathcal{M} and $\tilde{\mathcal{M}}$ be Riemannian manifolds with corresponding Riemannian metrics g and \tilde{g} , respectively. A smooth local embedding $f : \mathcal{M} \rightarrow \tilde{\mathcal{M}}$ is *conformal* if it preserves

orientations and there exists a $u : \mathcal{M} \rightarrow \mathbb{R}$ satisfying:

$$\tilde{g}_{f(p)}(df_p(v), df_p(w)) = e^{2u(p)} \cdot g_p(v, w), \quad (3)$$

for all points $p \in \mathcal{M}$ and tangent vectors $v, w \in T_p\mathcal{M}$. The function u is called the *log conformal factor*. Intuitively, we can equivalently push forward v and w via the differential df_p and compute their inner product in the tangent space at $f(p)$, or we can compute the inner product of v and w in the tangent space at p and scale the product by $e^{2u(p)}$.

Analogously, consider a Euclidean triangle mesh $T = (V, E, F)$ with two embeddings f and \tilde{f} (e.g., one for the source manifold and one for the sphere), corresponding to discrete metrics ℓ and $\tilde{\ell}$, respectively. The metrics are (*discretely*) *conformally equivalent* (Springborn et al., 2008) if there is a function $u : V \rightarrow \mathbb{R}$ satisfying:

$$\tilde{\ell}_{ij} = e^{(u_i + u_j)/2} \cdot \ell_{ij}, \quad (4)$$

for all edges $(i, j) \in E$. As in the continuous case, the function u is also called the log conformal factor. Intuitively, $e^{2u_i} \in \mathbb{R}_{++}$ captures how differential area changes (multiplicatively) as the vertex $i \in V$ is sent from f_i to \tilde{f}_i .

Two important properties of discrete conformal equivalence are transitivity and invariance under Möbius transformations. First, suppose ℓ_1, ℓ_2 , and ℓ_3 are discrete metrics on the same triangle mesh. If ℓ_1 and ℓ_2 are discretely conformally equivalent with log conformal factor u_1 and ℓ_2 and ℓ_3 are discretely conformally equivalent with log conformal factor u_2 , then ℓ_1 and ℓ_3 are discretely conformally equivalent with log conformal factor $u_1 + u_2$. Second, if two vertex embeddings corresponding to the same mesh are related via a Möbius transformation (which includes Euclidean transformations, sphere inversions, and stereographic projections), then the corresponding discrete metrics are discretely conformally equivalent (Springborn et al., 2008).

3.1.2. SPHERICAL PARAMETRIZATIONS

Consider a triangle mesh $T = (V, E, F)$ that approximates a sphere, with vertex embedding f and discrete metric ℓ . Typically, such a mesh is circumscribed by the sphere, meaning the vertices lie on the sphere and the edges lie within. Our goal here is to transform each linear triangle surface in T into a spherical triangle (Figure 3). We use the following procedure (Springborn et al., 2008; Bobenko et al., 2016), which returns a new embedding \tilde{f} of T that maps the vertices to the sphere S^2 and corresponds to a discrete metric that is discretely conformally equivalent to ℓ :

1. Select an arbitrary vertex $i^* \in V$ to be removed,
2. Apply a change of discrete metric, making each neighbor of i^* equally distant from i^* (this metric is discretely conformally equivalent to ℓ),

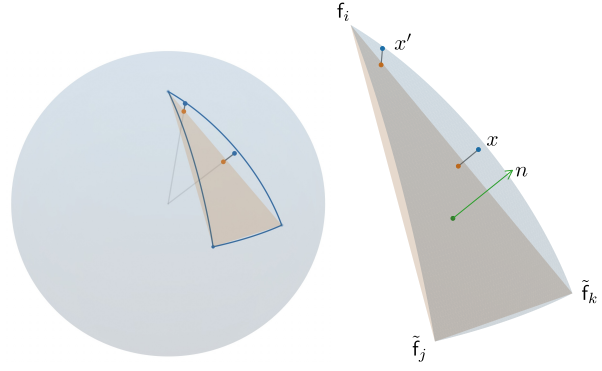


Figure 3. Correspondence between an inscribed Euclidean triangle and its associated spherical triangle. Points on the sphere are in blue, projected points (onto the inscribed triangles) are in orange, and the inscribed triangle normal vector is in green.

3. Remove i^* from V , and all incident edges from E and incident faces from F (yielding a topological disk),
4. Compute a *flat* discretely conformally equivalent metric via convex optimization which leaves the distances between boundary vertices unchanged,
5. Embed the vertices in the plane \mathbb{R}^2 with edge lengths determined by the new flat metric,
6. Stereographically project the vertices onto the unit sphere S^2 (through the north pole), maintaining discrete conformal equivalence of metrics,
7. Reinsert i^* at the north pole, along with removed edges and faces,
8. Apply Möbius transformations that map the sphere to itself (Lorentz transformations) to move the center of the vertex positions to the origin, again maintaining discrete equivalence of metrics.

Through spherical parametrization, we establish correspondences between three surfaces: a piecewise linear surface described by f , a piecewise linear surface inscribed within the unit sphere and described by \tilde{f} , and the unit sphere itself. These correspondences are illustrated in Figure 2. Appendix A provides the full details of this procedure. The key ideas are to: (i) use a convex energy formulation to compute the flat metric (Step 4), and (ii) produce an interpolation of the conformal factor on the sphere.

3.1.3. MÖBIUS REGISTRATION

In order to completely relate two meshes of the same manifold (e.g., to pool their training data), we must align their representations. With the result of Section 3.1.2, two spherical parametrizations of the same mesh will differ only by a

rotation (Baden et al., 2018). The set of rotations is substantially easier to work with than the set of Lorentz transformations. This rotation can be found via harmonic analysis.

For two complex-valued functions on the sphere $f, g : S^2 \rightarrow \mathbb{C}$, we can define a correlation function $C : SO(3) \rightarrow \mathbb{C}$ on the rotation group $SO(3)$ as:

$$C(R) = \int_{S^2} f(x) \overline{g(R^\top x)} dx, \quad (5)$$

for all rotation matrices $R \in SO(3)$. If f and g are real-valued, then so is C , and we can seek its global maximizer. The spherical harmonic transform (Kostelec & Rockmore, 2008) yields coefficients such that:

$$\begin{aligned} f(x) &= \sum_{l=0}^{\infty} \sum_{m=-l}^l \hat{f}_{lm} Y_l^m(x), \\ g(x) &= \sum_{l=0}^{\infty} \sum_{m=-l}^l \hat{g}_{lm} Y_l^m(x), \end{aligned} \quad (6)$$

for all $x \in S^2$, where $Y_l^m : S^2 \rightarrow \mathbb{C}$ denotes the spherical harmonic of l and order m . The $SO(3)$ Fourier transform of C can then be written in terms of the spherical harmonic transforms of f and g , as:

$$C(R) = \sum_{l=0}^{\infty} \sum_{m=-l}^l \sum_{m'=-l}^l \hat{f}_{lm} \overline{\hat{g}_{lm'}} \cdot \overline{D_{mm'}^l(R)}, \quad (7)$$

for all rotations $R \in SO(3)$, where $D_{mm'}^l$ denotes a Wigner D -function (Kostelec & Rockmore, 2008). Intuitively, the coefficients of Equation (7) are degree-wise outer products of the coefficients comprising each degree of the spherical harmonic transforms of f and g .

While evaluating C at any rotation is computationally difficult, Kostelec & Rockmore (2008) provide a fast method using a grid of Euler angles. This method makes use of the fast spherical harmonic transform, sampling f and g onto a spherical grid. We found a 64×64 spherical grid (a bandwidth of 32) to be sufficient for our experiments.

3.2. Differential Change of Area

For $l \in \{1, \dots, n\}$, consider a data point $x \in \tilde{\mathcal{D}}^{(l)}$. The data point x is mapped from the sphere to $M^{(l)}$ (the inverse transformation) in three stages; first x is mapped onto a Euclidean triangle of $\tilde{M}_{\text{inscr}}^{(l)}$, then rotated by the inverse rotation $R^{(l)\top}$ to lie on $M_{\text{inscr}}^{(l)}$, and finally moved to the point on $M^{(l)}$ with the same barycentric coordinates in the corresponding face. The rotation is isometric, incurring no change of area, and the final map from $M_{\text{inscr}}^{(l)}$ to $M^{(l)}$ is piecewise linear, incurring a multiplicative change of area equal to the area ratio of corresponding triangles (original triangle area divided by inscribed triangle area).

The first mapping, however, is nonlinear. To compute the corresponding change of area, suppose x is in the spherical triangle characterized by $(i, j, k) \in F^{(l)}$, where $F^{(l)}$ is the set of faces in $T^{(l)}$. Let n denote the normalized cross product of edge vectors in the face (yielding a unit normal vector), with:

$$n = \frac{(\tilde{f}_j^{(l)} - \tilde{f}_i^{(l)}) \times (\tilde{f}_k^{(l)} - \tilde{f}_i^{(l)})}{\|(\tilde{f}_j^{(l)} - \tilde{f}_i^{(l)}) \times (\tilde{f}_k^{(l)} - \tilde{f}_i^{(l)})\|_2}. \quad (8)$$

From Equation (19), we find that x is mapped to:

$$y = \frac{n^\top \tilde{f}_i^{(l)}}{n^\top x} \cdot x, \quad (9)$$

with Jacobian matrix given as:

$$\frac{dy}{dx} = \frac{(n^\top x)(n^\top \tilde{f}_i^{(l)})I_3 - (n^\top \tilde{f}_i^{(l)})xn^\top}{(n^\top x)^2}. \quad (10)$$

Now, consider any tangent vector to the sphere $v \in \mathbb{R}^3$, with $x^\top v = 0$. Suppose additionally that v has unit magnitude. The cross product $x \times v$ is another tangent vector, the result of rotating v in the tangent plane counterclockwise by a quarter turn. The pair $(v, x \times v)$ form an orthonormal basis for the tangent plane, and the triple $(v, x \times v, x)$ forms a right-handed orthonormal basis for \mathbb{R}^3 . The parallelogram spanned by v and $x \times v$ is a square with area 1, so we can compute the multiplicative change of area incurred when mapping x to y simply by computing the area of the parallelogram obtained by pushing forward v and $x \times v$ by the Jacobian dy/dx . This area is:

$$\begin{aligned} & \left\| \left(\frac{dy}{dx} \cdot v \right) \times \left(\frac{dy}{dx} \cdot (x \times v) \right) \right\|_2 \\ &= \frac{(n^\top \tilde{f}_i^{(l)})^2}{(n^\top x)^4} \cdot \left\| ((n^\top x)v - (n^\top v)x) \right. \\ & \quad \left. \times ((n^\top x)(x \times v) - n^\top(x \times v)x) \right\|_2 \\ &= \frac{(n^\top \tilde{f}_i^{(l)})^2}{|n^\top x|^3} \cdot \left\| (x^\top n)x + ((x \times v)^\top n)(x \times v) \right. \\ & \quad \left. + (v^\top n)v \right\|_2 \\ &= \frac{(n^\top \tilde{f}_i^{(l)})^2}{|n^\top x|^3}. \end{aligned} \quad (11)$$

The last equality follows since the term inside the norm is just the sum of the projections of n onto x , $x \times v$, and v ; since these three vectors form an orthonormal basis, the resulting sum has unit norm. Since:

$$((\tilde{f}_j^{(l)} - \tilde{f}_i^{(l)}) \times (\tilde{f}_k^{(l)} - \tilde{f}_i^{(l)}))^\top \tilde{f}_i^{(l)} = (\tilde{f}_j^{(l)} \times \tilde{f}_k^{(l)})^\top \tilde{f}_i^{(l)}, \quad (12)$$

we can write the final expression in Equation (11) as:

$$\frac{((\tilde{f}_j^{(l)} \times \tilde{f}_k^{(l)})^\top \tilde{f}_i^{(l)})^2 \cdot \|(\tilde{f}_j^{(l)} - \tilde{f}_i^{(l)}) \times (\tilde{f}_k^{(l)} - \tilde{f}_i^{(l)})\|_2}{\|((\tilde{f}_j^{(l)} - \tilde{f}_i^{(l)}) \times (\tilde{f}_k^{(l)} - \tilde{f}_i^{(l)}))^\top x\|^3}, \quad (13)$$

where the norm in the numerator is the area of the inscribed triangle characterized by (i, j, k) .

To summarize, the differential change of area when mapping x from the sphere to $M^{(l)}$ is, as a multiplicative factor, the product of Equation (14) and the ratio of areas for face (i, j, k) , represented both in $M^{(l)}$ and $M_{\text{inscr}}^{(l)}$. Using the observation about the norm from Equation (13), this differential change of area is:

$$\Delta^{(l)} \triangleq \frac{((\tilde{f}_j^{(l)} \times \tilde{f}_k^{(l)})^\top \tilde{f}_i^{(l)})^2 \|(\mathbf{f}_j^{(l)} - \mathbf{f}_i^{(l)}) \times (\mathbf{f}_k^{(l)} - \mathbf{f}_i^{(l)})\|_2}{|((\tilde{f}_j^{(l)} - \tilde{f}_i^{(l)}) \times (\tilde{f}_k^{(l)} - \tilde{f}_i^{(l)}))^\top x|^3}, \quad (14)$$

where now the norm in the numerator is instead the area of the triangle characterized by (i, j, k) in the original mesh.

3.3. Technical Description of Our Solution

We can now fully instantiate Algorithm 1. In Step 1, we spherically parametrize each of the piecewise linear surfaces, obtaining piecewise linear surfaces $M_{\text{inscr}}^{(1)}, \dots, M_{\text{inscr}}^{(n)}$ inscribed within the unit sphere and log conformal factor interpolations $\bar{u}^{(1)}, \dots, \bar{u}^{(n)} : S^2 \rightarrow \mathbb{R}$. For $i \in \{2, \dots, n\}$, we approximate the maximum correlation rotation matrix $R^{(i)} \in SO(3)$, maximizing the correlation function:

$$C^{(i)}(R) = \int_{S^2} \bar{u}^{(1)}(x) \bar{u}^{(i)}(R^\top x) dx, \quad (15)$$

over all rotation matrices $R \in SO(3)$. With identity rotation $R^{(1)} = I_3$, we rotate each of the inscribed surfaces by the corresponding rotation, obtaining rotated surfaces $\tilde{M}_{\text{inscr}}^{(1)}, \dots, \tilde{M}_{\text{inscr}}^{(n)}$. In Step 2, we map each data point in each $\mathcal{D}^{(i)}$ to $\tilde{M}_{\text{inscr}}^{(i)}$ and normalize the result to lie on the unit sphere, obtaining a spherical dataset $\tilde{\mathcal{D}}^{(i)}$.

We can now aggregate the spherical datasets and train a generative model using the resulting dataset (Step 3). However, to train such models with maximum likelihood estimation on the original surfaces $M^{(1)}, \dots, M^{(n)}$, we require the corresponding changes of area incurred by each of the maps to the unit sphere (Step 4). When evaluating log probability densities via a generative model on the sphere, we must subsequently subtract the log changes of area to compute log probability densities (corresponding to dividing density by change of area) on the original surface.

Elaborating on this point, suppose we choose a generative model on the sphere with density $\rho : S^2 \rightarrow \mathbb{R}_+$. For a dataset $\tilde{\mathcal{D}}^{(1)} \cup \dots \cup \tilde{\mathcal{D}}^{(n)}$ comprised of aligned spherical datasets, the data log likelihood (under the spherical density) is:

$$\sum_{l=1}^n \sum_{x \in \tilde{\mathcal{D}}^{(l)}} \log \rho(x). \quad (16)$$

while the corrected data log likelihood (under the corre-

sponding mesh densities) is simply:

$$\sum_{l=1}^n \sum_{x \in \tilde{\mathcal{D}}^{(l)}} \left(\log \rho(x) - \log \Delta^{(l)}(x) \right), \quad (17)$$

where $\Delta^{(l)}(x)$ denotes the change of area from Equation (14) for data point $x \in \tilde{\mathcal{D}}^{(l)}$. Note that the change of area terms only need to be computed once at the start of training for such a generative model via likelihood maximization; the only terms which cannot be precomputed include ρ , as this density changes throughout training.

The remaining Step 5 is to choose an appropriate generative model to train on the sphere, which we discuss next.

3.4. Choosing a Base Generative Model

Step 5 in Algorithm 1, in principle one could choose any Riemannian generative model that trains on canonical manifolds such as the unit sphere. In this paper, we instantiate our framework using two approaches: Riemannian continuous normalizing flows (CNFs) (Mathieu & Nickel, 2020) and Moser flows (Rozen et al., 2021), which we discuss in detail in Section B.

One issue we encountered is determining a good projection of a Euclidean gradient (which is the native gradient representation of many flow-based generative models) onto the sphere. A bad projection can lead to numerical instability and longer computational costs. For all of our base generative models, we adopt the approach of Rozen et al. (2021) using a normalizing trick discussed in Section B.1.

4. Experiments

We first demonstrate our method without the need for spherical alignment. We demonstrate our approach on 8 different meshes (see Table 1), which is significantly more than has been empirically demonstrated by other Riemannian generative modeling approaches. We train continuous normalizing flows and Moser flows on each mesh. The meshes and data used are from the ContactDB dataset (Brahmbhatt et al., 2019). Second, we show how our approach enables the sharing of data from distinct meshes approximating the same underlying manifold. We generate 5 similar but distinct meshes (derived from `stanford-bunny`) to show how a single generative model can be trained using several meshes corresponding to the same underlying manifold. We show that log likelihood tested on a held-out mesh improves with additional data, even when the data comes from different meshes. We also show how all 5 meshes can be used to simultaneously generate data on each of the 5 meshes. All experiments were run on a single NVIDIA RTX A6000 GPU. In all experiments, noise distributions are uniform on the sphere. Our code is available at github.com/vdorbs/spherical-generative-modeling.git

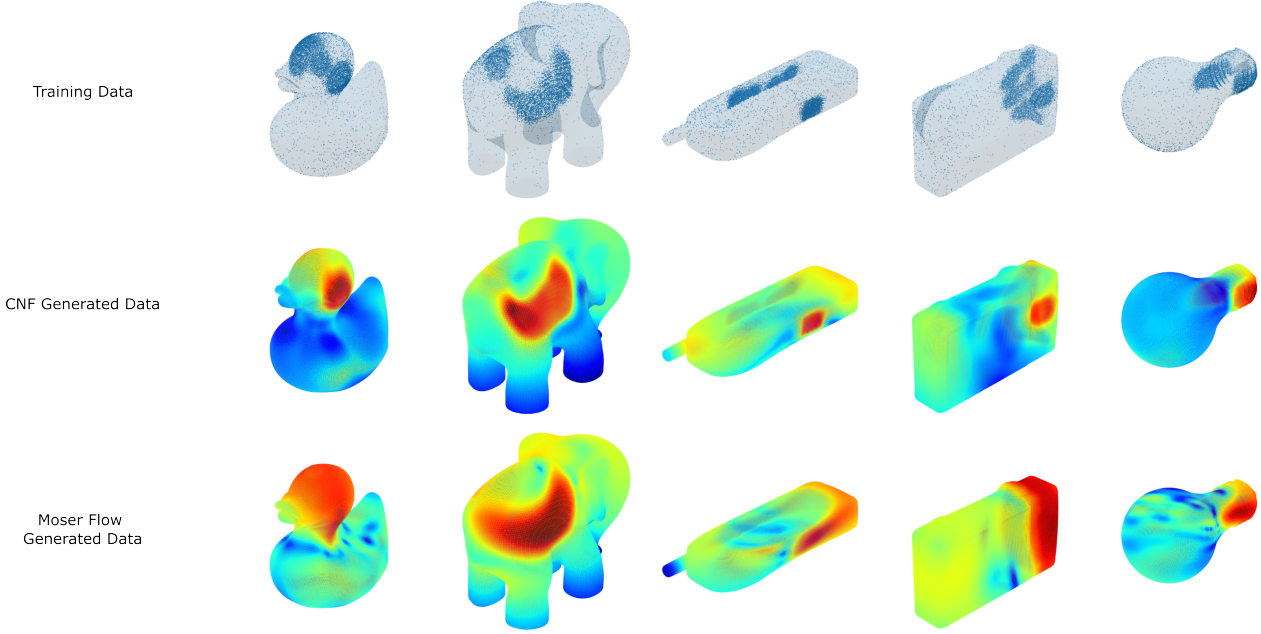


Figure 4. Showing five meshes: training data (top row), learned CNF densities (middle row), and learned Moser flow densities (bottom row). From left to right, the meshes are rubber-duck, elephant, cell-phone, camera, and light-bulb.

4.1. Training Data

ContactDB (Brahmbhatt et al., 2019) is a collection of grasping and manipulation data for applications in human-robot interaction. The data were collected by thermally imaging 3D printed household objects after they were grasped by human subjects. We study 8 objects, each handled by a single participant. The data take the form of triangle meshes with a single feature (intensity) at each vertex, indicating thermal energy transferred to the object. As in (Brahmbhatt et al., 2019), we process the contact maps by passing the intensities through a sigmoid function, assigning 0.999 probability to the maximum intensity and 0.001 to the minimum. As in (Rozen et al., 2021), we average the corresponding probabilities on each face to obtain an unnormalized probability distribution over faces. We then draw 10000 samples from each mesh, each sample generated by sampling a face according to the unnormalized distribution, then by sampling a uniformly distributed point on the sampled face.

4.2. Distribution Modeling Results

We run 5 trials for each of the 8 meshes, training both a CNF and a Moser flow. Validation results are listed in Table 1. In both cases we use 5000 training samples and 5000 validation samples. The CNF vector field and Moser flow flux field are both parametrized as 3-hidden layer neural networks with hidden dimensions of 32 and tanh nonlinearities. The inputs to both neural networks are vectors in \mathbb{R}^3 , with the CNF taking a fourth input of time. Both models

Table 1. Log likelihoods for 8 meshes (higher is better), averaged over 5 runs per mesh, plus or minus one standard deviation.

MESH	CNF	MOSER FLOW
CAMERA	4 ± 0.01703	3.726 ± 0.1048
STANFORD-BUNNY	4.354 ± 0.0435	4.168 ± 0.1937
LIGHT-BULB	4.44 ± 0.04114	4.239 ± 0.07521
ELEPHANT	4.472 ± 0.01215	4.462 ± 0.0361
MOUSE	4.769 ± 0.009795	4.726 ± 0.06756
CELL-PHONE	5.465 ± 0.01964	5.302 ± 0.1207
RUBBER-DUCK	5.75 ± 0.007362	5.368 ± 0.1799
BANANA	6.591 ± 0.02889	6.318 ± 0.1723

are trained with the Adam optimizer (Kingma & Ba, 2014). The CNF is trained for 100 epochs with a batch size of 256 and a learning rate of 10^{-2} . The Moser flow is trained for 4000 epochs with a batch size of 256 and a learning rate of 10^{-4} . These results show that our approach can reliably model distributions on multiple manifolds using multiple Riemannian generative models as subroutines.

4.3. Spherical Alignment

We next demonstrate our method when we have access to data on distinct meshes. For a single mesh, we sample data as in Section 4.1. We generate 5 distinct meshes by sampling 5 sets of vertices at random, each with only 1% of the vertices in the original mesh. The meshes are then obtained from Poisson surface reconstruction (Kazhdan et al., 2006)

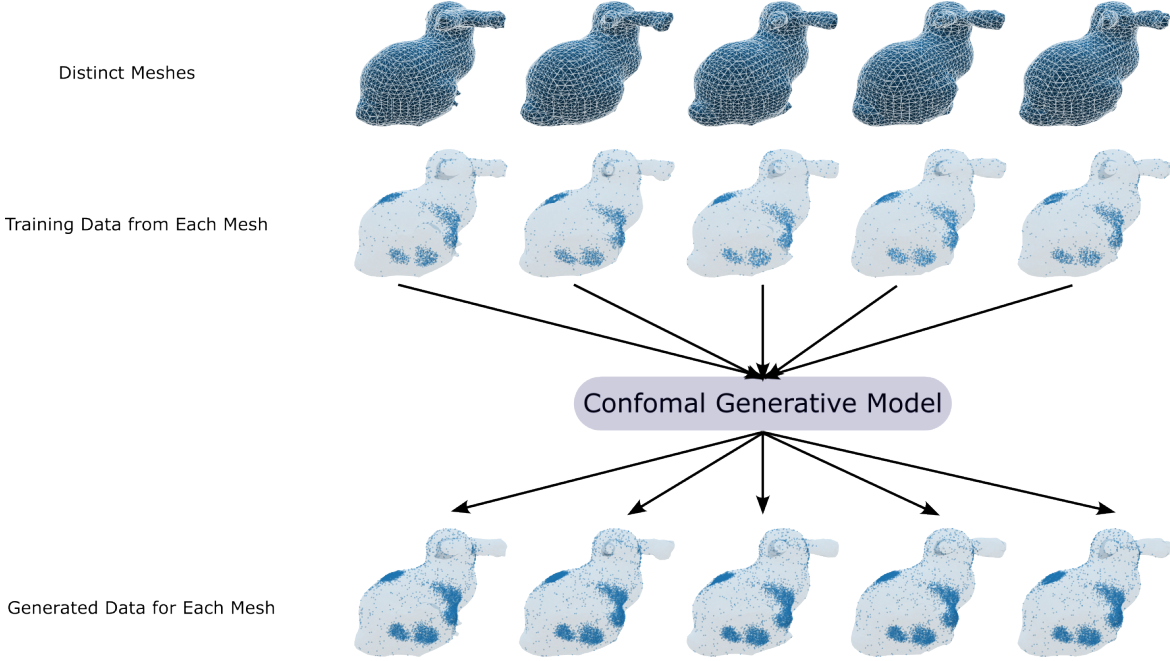


Figure 5. Distinct meshes (top row), training data on each mesh (second row) and samples generated from learned model (bottom row). The same model is used to generate data on each of the five meshes, trained using data aggregated from all meshes.

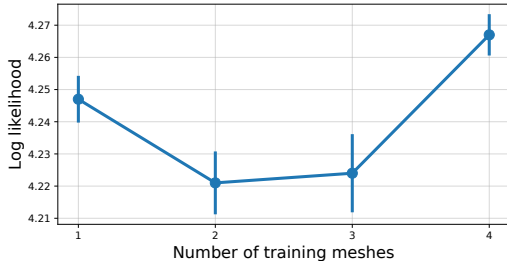


Figure 6. Performance of generative model on held-out mesh as more meshes and data are added.

with each point cloud. As reconstruction requires normal vectors at each point in a cloud, we use the vertex normals derived from the original mesh at each point rather than estimate normals from nearest neighbor tangent planes. The data from the original mesh is then partitioned into 5 equal subsets, with each subset projected onto a corresponding reconstructed mesh.

First, we hold out data from one mesh and run 20 trials training a CNF with data from 1, 2, 3, and all 4 of the remaining meshes. Each mesh has 2000 training data samples; we only use the first 1000 from each. Log likelihoods of data on the held-out mesh are shown in Figure 6. The CNF used has the same training configuration as in Section 4.2.

Second, we train a single conformal generative model that can generate data on each of the five meshes. We use data

from each of the five meshes to train the model, again using 1000 training samples and 1000 validation samples from each mesh. Generated samples are visualized in Figure 5. The CNF used has the same training configuration. These results demonstrate that data can be shared between distinct meshes for improved training, and that such models can readily generate data on qualitatively similar but unseen meshes.

5. Other Related Work

Generative Modeling on Meshes. The concurrent work of [Chen & Lipman \(2023\)](#) adopts a flow matching approach to generative modeling on Riemannian manifolds and, as a special case, triangle meshes. In this paradigm, a vector field is trained to match an average (weighted by the data distribution) of conditional vector fields, which are chosen for their relative simplicity. For triangle meshes, the conditional vector fields are constructed using kernel functions encoding approximate spectral distances. Both training and generation with the trained model require solving ODEs directly on the meshes, which can be difficult for complicated geometries.

Generative Modeling on Implicit Surfaces. An alternative approach to generative modeling on complicated manifolds is to use a learned signed distance function (SDF) ([Rozen et al., 2021](#)), which defines an implicit surface (i.e., the SDF is zero if the point is on the surface). In general,

learning SDFs can be quite complicated, and also lead to uncontrolled approximations of the original manifold. In contrast, our framework sidesteps this issue by leveraging tools in computational geometry.

Conformal Embedding Flows. Conformal transformations have also been applied to generative modeling problems in high dimensions under the manifold hypothesis (Ross & Cresswell, 2021). In this case, a (left) invertible map from a low-dimensional latent space to a high-dimensional data space must be learned jointly with a normalizing flow. The embedding is required to be conformal to tractably compute the corresponding change of density; this puts restrictions on the architecture used for manifold learning. Also, as with learning SDFs, manifold learning can be complicated with uncontrolled approximations of the original manifold.

Conformal Prediction. The term “conformal” is also used in the context of conformal prediction (Shafer & Vovk, 2008). Both conformal prediction and conformal geometry use a measure of how conformal a point is under a transformation – the former in terms of statistical calibration and the latter in terms of geometrical calibration. Otherwise, the two lines of research are unrelated.

References

- Baden, A., Crane, K., and Kazhdan, M. Möbius registration. In *Computer Graphics Forum*, volume 37, pp. 211–220. Wiley Online Library, 2018.
- Bobenko, A. I., Sechelmann, S., and Springborn, B. Discrete conformal maps: Boundary value problems, circle domains, fuchsian and schottky uniformization. In *Advances in Discrete Differential Geometry*, pp. 1–56. Springer, Berlin, Heidelberg, 2016.
- Brahmbhatt, S., Ham, C., Kemp, C. C., and Hays, J. Contactdb: Analyzing and predicting grasp contact via thermal imaging. In *Proceedings of the IEEE/CVF conference on computer vision and pattern recognition*, pp. 8709–8719, 2019.
- Brehmer, J. and Cranmer, K. Flows for simultaneous manifold learning and density estimation. *Advances in Neural Information Processing Systems*, 33:442–453, 2020.
- Chen, M., Tu, B., and Lu, B. Triangulated manifold meshing method preserving molecular surface topology. *Journal of Molecular Graphics and Modelling*, 38:411–418, 2012.
- Chen, R. T. and Lipman, Y. Riemannian flow matching on general geometries. *arXiv preprint arXiv:2302.03660*, 2023.
- Chen, R. T., Rubanova, Y., Bettencourt, J., and Duvenaud, D. K. Neural ordinary differential equations. *Advances in neural information processing systems*, 31, 2018.
- Crane, K. Conformal Geometry of Simplicial Surfaces. In *Proceedings of Symposia in Applied Mathematics*. American Mathematical Society, 2020.
- De Bortoli, V., Mathieu, E., Hutchinson, M., Thornton, J., Teh, Y. W., and Doucet, A. Riemannian score-based generative modeling. *arXiv preprint arXiv:2202.02763*, 2022.
- Dinh, L., Sohl-Dickstein, J., and Bengio, S. Density estimation using real nvp. *arXiv preprint arXiv:1605.08803*, 2016.
- Feiten, W., Lang, M., and Hirche, S. Rigid motion estimation using mixtures of projected gaussians. In *Proceedings of the 16th International Conference on Information Fusion*, pp. 1465–1472. IEEE, 2013.
- Gao, A., Castellanos, J., Yue, Y., Ross, Z., and Bouman, K. Deepgem: Generalized expectation-maximization for blind inversion. *Advances in Neural Information Processing Systems*, 34:11592–11603, 2021.
- Gerber, S., Tasdizen, T., Fletcher, P. T., Joshi, S., Whitaker, R., Initiative, A. D. N., et al. Manifold modeling for brain population analysis. *Medical image analysis*, 14(5): 643–653, 2010.
- Gillespie, M., Springborn, B., and Crane, K. Discrete conformal equivalence of polyhedral surfaces. *ACM Transactions on Graphics*, 40(4), 2021.
- Katsman, I., Lou, A., Lim, D., Jiang, Q., Lim, S. N., and De Sa, C. M. Equivariant manifold flows. *Advances in Neural Information Processing Systems*, 34:10600–10612, 2021.
- Kazhdan, M., Bolitho, M., and Hoppe, H. Poisson surface reconstruction. In *Proceedings of the fourth Eurographics symposium on Geometry processing*, volume 7, 2006.
- Kingma, D. P. and Ba, J. Adam: A method for stochastic optimization. *arXiv preprint arXiv:1412.6980*, 2014.
- Kostelec, P. J. and Rockmore, D. N. Ffts on the rotation group. *Journal of Fourier analysis and applications*, 14(2):145–179, 2008.
- Lou, A., Lim, D., Katsman, I., Huang, L., Jiang, Q., Lim, S. N., and De Sa, C. M. Neural manifold ordinary differential equations. *Advances in Neural Information Processing Systems*, 33:17548–17558, 2020.
- Mathieu, E. and Nickel, M. Riemannian continuous normalizing flows. *Advances in Neural Information Processing Systems*, 33:2503–2515, 2020.

- Papamakarios, G., Nalisnick, E. T., Rezende, D. J., Mohamed, S., and Lakshminarayanan, B. Normalizing flows for probabilistic modeling and inference. *J. Mach. Learn. Res.*, 22(57):1–64, 2021.
- Rezende, D. and Mohamed, S. Variational inference with normalizing flows. In *International conference on machine learning*, pp. 1530–1538. PMLR, 2015.
- Ross, B. and Cresswell, J. Tractable density estimation on learned manifolds with conformal embedding flows. *Advances in Neural Information Processing Systems*, 34: 26635–26648, 2021.
- Rozen, N., Grover, A., Nickel, M., and Lipman, Y. Moser flow: Divergence-based generative modeling on manifolds. *Advances in Neural Information Processing Systems*, 34:17669–17680, 2021.
- Shafer, G. and Vovk, V. A tutorial on conformal prediction. *Journal of Machine Learning Research*, 9(3), 2008.
- Shapovalov, M. V. and Dunbrack Jr, R. L. A smoothed backbone-dependent rotamer library for proteins derived from adaptive kernel density estimates and regressions. *Structure*, 19(6):844–858, 2011.
- Sohl-Dickstein, J., Weiss, E., Maheswaranathan, N., and Ganguli, S. Deep unsupervised learning using nonequilibrium thermodynamics. In *International Conference on Machine Learning*, pp. 2256–2265. PMLR, 2015.
- Song, J., Yu, L., Neiswanger, W., and Ermon, S. A general recipe for likelihood-free bayesian optimization. In *International Conference on Machine Learning*, pp. 20384–20404. PMLR, 2022.
- Song, Y., Sohl-Dickstein, J., Kingma, D. P., Kumar, A., Ermon, S., and Poole, B. Score-based generative modeling through stochastic differential equations. In *International Conference on Learning Representations*, 2020.
- Song, Y., Shen, L., Xing, L., and Ermon, S. Solving inverse problems in medical imaging with score-based generative models. *arXiv preprint arXiv:2111.08005*, 2021.
- Springborn, B., Schröder, P., and Pinkall, U. Conformal equivalence of triangle meshes. In *ACM SIGGRAPH 2008 papers*, pp. 1–11. 2008.
- Wang, S., Wang, Y., Jin, M., Gu, X., and Samaras, D. 3d surface matching and recognition using conformal geometry. In *2006 IEEE Computer Society Conference on Computer Vision and Pattern Recognition (CVPR’06)*, volume 2, pp. 2453–2460. IEEE, 2006.

A. Details on Spherical Parameterization

Here we expand on the spherical parameterization procedure outlined in Section 3.1.2.

To compute the flat metric, permitting a planar vertex embedding, we minimize the convex energy in Equation 7 of Springborn et al. (2008), a function of the corresponding log conformal factor. We minimize the energy with second-order optimization (Newton’s method), where the gradient of the energy simply measures the defect of the sum of angles around each vertex from 2π (or π for boundary vertices) and the Hessian is the (cotangent) Laplacian of the triangle mesh. When the gradient is 0, the sum of the angles around each interior vertex is exactly 2π , which is the required curvature of a flat surface. The boundary edge lengths are unchanged by imposing 0 boundary conditions during optimization.

The domain over which the convex energy is optimized includes log conformal factors corresponding to discrete metrics that violate the triangle inequality, meaning it is possible to find a solution which cannot be used to embed vertices in the plane. (Springborn et al., 2008) propose flipping edges when such violations are detected, and many follow-up works have investigated this problem further, see (Gillespie et al., 2021) for a complete discussion and solution. However, we did not encounter such problems in our experiments.

The Möbius transformations moving the center of the vertex positions can be computed using either (Bobenko et al., 2016) or (Baden et al., 2018); we used the latter, which adds weights to the vertex positions based on corresponding triangle areas from the original mesh.

Denote the discrete metric corresponding to \tilde{f} by $\tilde{\ell}$. As a byproduct of this procedure, we also obtain the log conformal factor u which establishes discrete conformal equivalence between ℓ and $\tilde{\ell}$. We refer to \tilde{f} as a spherical parametrization of T .

Through spherical parametrization, we establish correspondences between three surfaces: a piecewise linear surface described by f , a piecewise linear surface inscribed within the unit sphere and described by \tilde{f} , and the unit sphere itself. These correspondences are illustrated in Figure 2. We move between the piecewise linear surfaces via barycentric coordinates within each face (this transformation is also piecewise linear). To move from the surface inscribed within the sphere to the sphere itself, we simply normalize points to have unit norm. To move in the opposite direction (from the sphere to the surface inscribed within the sphere), we compute the intersection of the ray from the origin in the direction of a query point and the inscribed surface. Specifically, if $x \in S^2$ is a query point located in the spherical triangle characterized by $(i, j, k) \in F$, then the intersection $\alpha x \in \mathbb{R}^3$ (for some scalar $\alpha \in [0, 1]$) with the inscribed surface satisfies:

$$((\tilde{f}_j - \tilde{f}_i) \times (\tilde{f}_k - \tilde{f}_i))^\top (\alpha x - \tilde{f}_i) = 0, \quad (18)$$

where the cross product $(\tilde{f}_j - \tilde{f}_i) \times (\tilde{f}_k - \tilde{f}_i)$ is perpendicular to the inscribed Euclidean triangle characterized by (i, j, k) . Rearranging terms, we have:

$$\alpha = \frac{((\tilde{f}_j - \tilde{f}_i) \times (\tilde{f}_k - \tilde{f}_i))^\top \tilde{f}_i}{((\tilde{f}_j - \tilde{f}_i) \times (\tilde{f}_k - \tilde{f}_i))^\top x} = \frac{(\tilde{f}_j \times \tilde{f}_k)^\top \tilde{f}_i}{((\tilde{f}_j - \tilde{f}_i) \times (\tilde{f}_k - \tilde{f}_i))^\top x}. \quad (19)$$

This latter correspondence is illustrated in Figure 2.

With these correspondences established, we denote the two piecewise linear surfaces as $M \subset \mathbb{R}^d$ and $M_{\text{inscr}} \subset \mathbb{R}^3$, respectively. We also generate an interpolation of the log conformal factor u as a function on the sphere, $\tilde{u} : S^2 \rightarrow \mathbb{R}$. To compute the interpolated value $\tilde{u}(x)$ at a query point $x \in S^2$, we first project x onto M_{inscr} using Equation (19); we then interpolate the values of u at the vertices of the intersected triangle using the corresponding barycentric coordinates as interpolation weights.

B. Details on Base Generative Models

B.1. Riemannian Continuous Normalizing Flows

In the sections that follow, for convenience we adopt the convention of diffusion and score-based generative models (Sohl-Dickstein et al., 2015; Song et al., 2020), for which the *forward* direction of a generative model maps a data distribution to a noise distribution.

In the Euclidean setting, a *continuous normalizing flow* (CNF) (Chen et al., 2018) is characterized by a parametric time-varying vector field $f : \mathbb{R}^d \times [0, 1] \rightarrow \mathbb{R}^d$. For an initial probability density $\rho_0 : \mathbb{R}^d \rightarrow \mathbb{R}_+$, the time-varying density

$\rho : \mathbb{R}^d \times [0, 1] \rightarrow \mathbb{R}_+$ solving (with initial condition ρ_0) the probability mass continuity equation:

$$\frac{\partial \rho}{\partial t} + \operatorname{div}(\rho \cdot f) = 0, \quad (20)$$

describes how the probability density of a random initial condition (distributed according to ρ_0) evolves subject to the vector field f . The product $\rho \cdot f$ is the *probability mass flux*, and its divergence can be expanded as:

$$\operatorname{div}(\rho \cdot f) = \nabla \rho^\top f + \rho \cdot \operatorname{div} f. \quad (21)$$

This form allows us to express the rate of change of (log) probability density along deterministic trajectories governed by the vector field f . That is, for $x \in \mathbb{R}^d$ and a trajectory $\gamma : [0, 1] \rightarrow \mathbb{R}^d$ satisfying:

$$\frac{d\gamma}{dt} = f(\gamma(t), t), \quad (22)$$

for all $t \in (0, 1)$, we also have (from [Chen et al. \(2018\)](#)):

$$\frac{d}{dt} \log \rho(\gamma(t), t) = -\operatorname{div}(\rho \cdot f)(\gamma(t), t). \quad (23)$$

This ordinary differential equations represented by Equation (22) and Equation (23) can be solved simultaneously. With this augmented system, we can map a data distribution to a noise distribution (solve forward) or a noise distribution to a data distribution (solve backward). Training the model requires querying log likelihoods of data; to compute likelihoods, data are propagated forward under Equation (22), the log probability densities of the corresponding terminal states (under a chosen noise distribution) are computed, and the terminal states and log probability densities are propagated backward under both Equation (22) and Equation (23).

From Euclidean to Spherical Gradients. In the spherical setting, vector fields specify tangent vectors. That is, at a point $x \in S^2$, a vector field specifies a tangent vector $v \in \mathbb{R}^3$ such that $x^\top v = 0$. We can compute differential operators like ∇ and div and solve ordinary differential equations by extending functions defined on the sphere to functions defined on all of $\mathbb{R}^3 \setminus \{0\}$ as in [Rozen et al. \(2021\)](#). Specifically, for tangent vector field $f : S^2 \times [0, 1] \rightarrow \mathbb{R}^3$ and probability density $\rho : S^2 \times [0, 1] \rightarrow \mathbb{R}_+$, we define extensions:

$$\tilde{f}(x, t) = f(x/\|x\|_2, t), \quad \tilde{\rho}(x, t) = \rho(x/\|x\|_2, t), \quad (24)$$

for all nonzero $x \in \mathbb{R}^3$ and times $t \in [0, 1]$. The spherical gradient of f is the Euclidean gradient of \tilde{f} . The spherical divergences of f and $\rho \cdot f$ are the respective Euclidean divergences of \tilde{f} and $\tilde{\rho} \cdot \tilde{f}$. As in [\(Rozen et al., 2021\)](#), we can solve Equation (22) by substituting f with \tilde{f} and deploying any differentiable (adaptive-step) Euclidean solver. Alternatively, we can solve Equation (22) using charts on the sphere ([Lou et al., 2020](#)), which locally represent the sphere and the vector field in Euclidean space (for example, by using spherical exponential and log maps). While this latter approach has the advantage of constructively restricting the solution of Equation (22) to the sphere, in our experiments the former approach maintained proximity to the sphere within tight tolerances.

B.2. Moser Flows

[Rozen et al. \(2021\)](#) bypass the need to solve ordinary differential equations to query log likelihoods by modeling the probability mass flux directly (as opposed to the vector field f) and restricting the class of vector fields used to generate data samples. For a data density $\mu : S^2 \rightarrow \mathbb{R}_+$ and a noise density $\nu : S^2 \rightarrow \mathbb{R}_+$, the probability mass flux is modeled as a parametric time-invariant tangent vector field $F : S^2 \rightarrow \mathbb{R}^3$ for which:

$$\mu(x) - \nu(x) = -\operatorname{div} F(x), \quad (25)$$

for all $x \in S^2$. That is, when ν is selected as well as parameters for F , the modeled data density is given by Equation (25). To generate data samples from noise, the vector field:

$$f(x, t) = \frac{F(x)}{\nu(x) + (1 - t) \cdot \operatorname{div} F(x)}, \quad (26)$$

is used, and the probability density solving the corresponding continuity equation is:

$$\rho(x, t) = (1 - t)\mu(x) + t\nu(x), \quad (27)$$

for all $x \in S^2$ and $t \in [0, 1]$. Note that this probability density interpolates linearly (in time) between μ and ν .

To ensure that the flux model corresponds to a valid probability density, the divergence of the flux field must integrate to 0 and be greater than $-\nu$ everywhere. The first requirement follows from the divergence theorem, replacing the integral of divergence with a boundary integral (where the boundary is empty). The second requirement must be enforced via an integral constraint, approximated with Monte Carlo integration (using a uniform samples from the original mesh).